Inverse Tapered AlGaN Micropillar and Nanowire LEDs for Improved Light Extraction Efficiency at 270 nm

Bryan Melanson, Matthew Seitz, and Jing Zhang

***Abstract*—Deep-ultraviolet (DUV) light emitting diodes (LEDs) show great potential in a wide range of applications, but suffer from poor external quantum efficiencies (EQEs) when compared to visible LEDs, due to their exceptionally poor light extraction efficiency (η_{EXT}). One successful method of improving the η_{EXT} of DUV LEDs is the use of micropillar and nanowire arrays. Our previous works have reported the development of an "inverse taper" profile in AlGaN micropillars during wet etching in heated hydroxyl-based chemistries. Here, we study the effects of inverse tapering on the η_{EXT} of AlGaN microstructures and nanostructures at 270 nm using finite-difference time-domain simulations, in accordance with our experimental results. Results show that η_{EXT} can be increased from ∼45% to more than 95% for TM-polarized emission in microstructures with diameters of 1 μm and heights >1 μm, and from ∼35% to more than 85% for TE-polarized emission by an inverse taper angle of 5°. Results for nanostructures also indicate significant η_{EXT} improvements through tuning of the inverse taper angle. These findings, along with our demonstration of inverse tapered high Al-content AlGaN micro and nanostructures, could enable the development of record-high EQE DUV LEDs based on arrays of high aspect ratio structures with high η_{EXT}.**

***Index Terms*—LED, GaN, AlGaN, light extraction, inverse taper, micropillar, nanowire, 270 nm.**

I. Introduction

DEEP-ultraviolet (DUV) light emitting diodes (LEDs) based on III-nitride materials show great potential for use in a variety of applications ranging from UV curing, 3D printing, photolithography, and remote sensing to water purification and surface sterilization [1], [2], [3], [4], [5]. Of particular note is the ability of certain DUV (200–280 nm) wavelengths to neutralize viruses, bacteria, and other pathogens, a capability which has gained considerable interest since the SARS-CoV-2 pandemic began in early 2020 [6]. The energies of DUV photons enable their absorption by the intercellular components of microbes, whereas longer wavelength UV photons (280–400 nm) tend to be more easily absorbed by the cell walls of these pathogens [6]. Photons which are absorbed in the intercellular regions of pathogens cause severe damage to their genomic systems, "inactivating" them such that they are no longer able to reproduce [6]. Recent research has shown that DUV wavelengths between 250 nm (4.96 eV) and 280 nm (4.43 eV) are most effective at inactivating pathogens, and that every microbe exhibits maximum susceptibility at different wavelengths within this range [6], [7], [8]. The unique response of different microbes to DUV light make LEDs the ideal means of generating DUV light for antimicrobial applications, since the emission wavelengths of DUV LEDs can be precisely tuned to target specific pathogens, whereas conventional UV lamps have fixed emission lines.

When compared with mercury lamps, the current most common UV light source, LEDs offer numerous benefits, including compact form factors, improved scalability, narrower linewidths and tunable emission wavelengths, rapid switching speed, much longer lifespans, and improved environmental compatibility [1], [2], [3], [4], [5]. Despite the numerous advantages of DUV LEDs over mercury lamps, they have not yet seen widespread adoption in most potential applications due to their relatively poor external quantum efficiencies (EQEs) which limit their maximum output power and make it difficult for them to compete with high power mercury lamps. Unlike visible (400–750 nm) LEDs based on the InGaN/GaN materials system which can have EQEs of up to 80% [9], DUV LEDs based on the AlGaN materials system often have EQEs of around 1% [1], [2], [3], [4], [5], with a record of 20% having been achieved at 275 nm [10]. Although recent research has produced massive improvements in the internal quantum efficiency (IQE) of DUV LEDs by improving *p*-type doping [1], [2], optimizing quantum well (QW) design [1], [2], and reducing the dislocation density in the QW [1], [2], [11], light extraction efficiency (η_{EXT}) remains the primary bottleneck preventing attainment of high EQEs. While IQEs of up to 85% have been demonstrated at 260 nm [12], η_{EXT} remains much lower, generally being limited to less than 20% at DUV wavelengths, in sharp contrast to the >90% η_{EXT} which can be obtained in blue LEDs [1], [13]. η_{EXT} is limited in DUV LEDs by several factors, including absorption of light by the narrower bandgap p-GaN contact layer which is needed to improve contact resistance and current spreading [14], [15], [16], reabsorption of emitted light by the epitaxial layers and substrate due to the high refractive index mismatch between AlGaN and air which leads to increased total internal reflection (TIR) [16],

Manuscript received 6 September 2022; revised 26 October 2022; accepted 6 November 2022. Date of publication 11 November 2022; date of current version 23 November 2022. This work was supported by the National Science Foundation under Award ECCS 1751675. *(Corresponding authors: Bryan Melanson; Jing Zhang.)*

The authors are with the Electrical and Microelectronic Engineering Department, Rochester Institute of Technology, Rochester, NY 14623 USA (e-mail: bcm9356@rit.edu; ms3897@rit.edu; jzeme@rit.edu).

Digital Object Identifier 10.1109/JPHOT.2022.3221353

and increased transverse-magnetic (TM) polarized emission at shorter wavelengths, which is more difficult to extract from planar LEDs than the transverse-electric (TE) polarized light which dominates at wavelengths greater than 300 nm [14], [16], [17].

A variety of approaches have been explored as means to improve the η_{EXT} of DUV LEDs, including the use of surface roughening and nanostructuring to reduce TIR [18], [19], [20], photonic crystal out-coupling [10], [15], high reflectivity contacts based on novel metal stacks [10], [21], transparent, low resistivity p-AlGaN layers to replace the p-GaN contact layer [10], [15], and nanowire/micropillar formation to reduce TIR and improve extraction of TM-polarized light [2], [14], [22], [23], [24], [25], [26], [27], [28], [29], [30], [31], [32], [33], [34], [35], [36], [37]. While many of these approaches have been shown to be moderately effective at improving η_{EXT}, nanowires and micropillars have been found to be the most effective [14], [16], [17], [22], [38], [39], [40]. Nanowires and micropillars increase the surface to volume ratio of the active region, making it much easier for light, especially TM-polarized light, to escape into free space. In addition to improving extraction efficiency, the high aspect ratio (AR) of these structures compared to conventional mesa LEDs has been shown to improve dopant concentration (particularly of the Mg p-dopant) due to enhanced surface doping [26], [41], [42] and allow for growth on non-conventional substrates and transfer to flexible substrate [43], [44], [45]. AlGaN nanowires are usually formed using a bottom up epitaxial growth approach where nanowires are nucleated on, and grown from a substrate using molecular beam epitaxy (MBE) or metal organic chemical vapor deposition (MOCVD) [26], [27], [28], [29], [30], [31], [32], [33], [34], [35], [36], [37]. An alternative approach is "top-down" fabrication, in which plasma dry-etching and lithography are used to form ordered arrays of high AR structures from a bulk epistack. While this approach is not as thoroughly explored for AlGaN LEDs emitting in the DUV range, it is well studied for longer wavelength LEDs and offers number of benefits over epitaxially grown structures. Top-down fabrication offers much greater control over array uniformity, improved nanowire/micropillar morphology, simplified electrical contact formation, and more scalable manufacturing.

We recently demonstrated the top-down fabrication and characterization of electrically driven micropillar array LEDs emitting at 286 nm [46]. This was the first demonstration of such devices using a top-down fabrication approach, and the narrow, 9 nm emission linewidth and output power densities of more than 35 mW/cm^2 make our devices competitive with epitaxially grown DUV nanowire LEDs [26], [27], [28], [29], [30], [31], [32], [33], [34], [35], [36], [37]. More details on the fabrication and testing of these devices can be found in Ref. [46]. In this prior work, we also reported that extended hydroxyl-based wet etches of AlGaN microstructures lead to development of an "inverse taper" profile, in which the bases of the microstructures eventually taper to a point, causing them to detach from the substrate completely [45], [46]. Etching of GaN and InGaN with hydroxyl-based chemistries such as potassium hydroxide (KOH) and tetramethylammonium hydroxide (TMAH) has been well studied, and is even used in industrial power electronics and LED manufacturing to remove dry etch damage and improve device efficiency [46], [47], [48], [49], [50], [51], [52], [53]. GaN and InGaN etch crystallographically in hydroxyl-based solutions, with the non-polar and semi-polar wurtzite planes etching rapidly while the polar c-plane has a negligibly slow etch rate [46], [47], [48], [49], [50]. High AR dry etched GaN and AlGaN structures generally have a "normal taper" profile where the base of the structure is slightly flared and has larger dimensions than the lithographically defined top diameter of the structure. Hydroxyl-based etches can be used to remove the unwanted flared bases of top-down fabricated nanowires and microstructures based on c-plane epitaxy as the etch will effectively self-terminate when a surface becomes perfectly vertical. In contrast to the well-studied behavior of this etch in GaN and InGaN, self-termination of the etch does not appear to occur in n-doped AlGaN with Al-content of ~50–70%, leading to development of an inverse taper profile with taper angle α which continually increases until the base of the structure narrows to a point and detaches from the substrate. Fig. 1 shows cross-sectional schematics and scanning electron microscope (SEM) images of our fabricated AlGaN micropillar structures with normal taper (no KOH etching), no taper (5 min KOH etching), and inverse taper (60 min KOH etching). KOH etching was performed in 40% AZ400K (a photoresist developer containing 2 wt% KOH) heated to 80 °C. More details on this fabrication process can be found in [46].

In this work, we investigate the effects of an inverse taper profile on the η_{EXT} of nanowires and micropillars emitting at 270 nm using finite-difference time-domain (FDTD) simulations in order to understand and study the η_{EXT} effects of inverse tapered structures (Fig. 1(c1), (c2)) over those with vertical sidewalls (Fig. 1(b1), (b2)). Previous simulation-based studies of DUV LEDs have shown that nanowires and other vertical structures can produce significant improvements in η_{EXT} when compared to conventional mesa structures with lateral dimensions (generally 20–1000 μm) far exceeding the mesa height (generally 100–500 nm) [14], [16], [17], [22], [38], [39], [40], [54]. These enhancements are shown to be much more pronounced for TM-polarized light, which has electric field vectors parallel to the epitaxial c-plane making it difficult to extract from mesa structures [14], [55]. Nanowires and micropillars with lateral dimensions (generally 100 nm–2 μm) equal to or much smaller than their height (generally 100 nm - 5 μm) allow TM-polarized light to easily escape through their sidewalls where the electric field vectors of TM-polarized photons are perpendicular to the AlGaN/air interface. For example, Ryu et al. showed through FDTD simulation that the η_{EXT} of TM-polarized light could be increased from 0.1% to more than 60% at 280 nm through use of nanorod structures with diameters of around 300 nm and heights of 1 μm, an astonishing 600 fold improvement [40]. Likewise, Ooi et al. showed that nanowires could improve TM- and TE-polarized η_{EXT} from 0.2% to 48% and 2% to 41% respectively, when compared to mesa LEDs emitting at 230 nm [14]. Given that differences in η_{EXT} between nanowires/micropillars and mesa LEDs are already well understood, this study focuses on the effects of nano and microstructure geometry, that is, the shapes and sizes of these structures, on TM- and TE-polarized

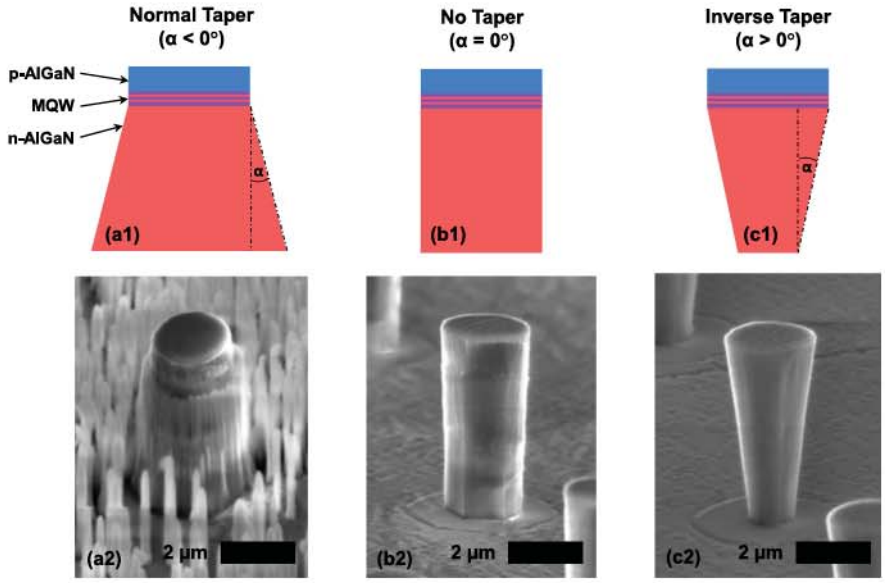

Fig. 1. Cross sectional schematics showing structures with normal taper (a1), no taper (b1), and inverse taper (c1), along with representative SEM images of each structure (a2)–(c2).

η_{EXT}. Many different parameters are considered, including structure height, diameter, taper angle, and polarization direction. We categorize structures based on their dimensions (D_s) as either nanostructures (100 nm $< D_s <$ 1 μm), or microstructures ($D_s >$ 1 μm).

II. Simulation Methodology

Three-dimensional (3D) FDTD simulations were used to explore the extraction efficiencies of AlGaN nano and microstructures at an emission wavelength of 270 nm. 270 nm was chosen as it lies at the center of DUV susceptibility range for most pathogens and is one of the most commonly explored DUV wavelengths, alongside 230 nm and 280 nm. 3D FDTD simulation has been used extensively to explore the propagation of light within the complex, multi-material structures found in LEDs, lasers, solar cells, and photodetectors [14], [16], [17], [22], [38], [39], [40], [54]. This method models the propagation of electromagnetic waves in the time domain within an arbitrarily defined spatial domain through direct solution of Maxwell's curl equations. In this sense, it is far more accurate, albeit slower, than ray tracing approaches because it allows for the interaction and interference of electromagnetic waves as well as the interaction of waves with the propagation medium and material interfaces. The spatial domain is divided into a non-uniform Yee mesh, with increased mesh resolution near material interfaces and reduced mesh resolution in bulk material to optimize simulation time and accuracy. More details on the FDTD method can be found in Refs. [56] and [57]. Our simulations were performed using Synopsys Fullwave, a commercial FDTD software package designed specifically for modelling the propagation of light in complex structures [58]. To set up a simulation in Fullwave a structure is first designed using a specialized 3D computer aided design (CAD) software called Rsoft-CAD which a part of the Fullwave software package. Different material types and properties can be assigned to each part of a structure to allow for the construction of complex, multi-material objects. Dipole sources are then placed manually with the structure, followed by monitor planes and volumes which can be set to capture a wide range of data including electric field intensity and luminous flux (power). TM-polarized light, which has its electric field component perpendicular to the c-axis ($\boldsymbol{E} \perp$ c-axis), is produced by a single double weighted linearly polarized dipole oriented along the z-axis, while TE-polarized light, which has its electric field component parallel to the c-axis ($\boldsymbol{E} \parallel$ c-axis), is produced using two single weighted linearly polarized dipoles, one with x-orientation and one with y-orientation.

Fig. 2 shows a cross-sectional representation of a simulated structure, which has its axis aligned with z-axis. Diameter is varied from 100 nm to 1.5 μm, height from 100 nm to 3.5 μm, and taper angle α from $-10°$ to $25°$. All structures have a circular cross section and fixed p-AlGaN and MQW layer thicknesses. A simulation domain in the shape of a rectangular prism is defined using perfectly matched layer (PML) boundary conditions, which act as perfectly absorbing interfaces to prevent reflection of incident electromagnetic waves. The bottom of the domain is located 200 nm below the surface of the bulk n-AlGaN, while the sides and top of the domain are located 500 nm from the foremost surfaces of the structure. The absorption coefficients of the AlGaN and MQW regions were assumed to be 10 cm^{-1} and 1000 cm^{-1}, respectively [17], [59], [60], [61], while refractive indices were likewise adapted from Refs. [17] and [59] to be 2.49 and 2.54 for the AlGaN and MQW regions respectively. The x, y, and z-oriented dipoles are placed on the axis of the structure directly in the center of the MQW layer. A cubic monitor with dimensions of 20 nanometers is placed to enclose the dipole sources and measure the full luminous flux of the dipoles while six planar power monitors are located

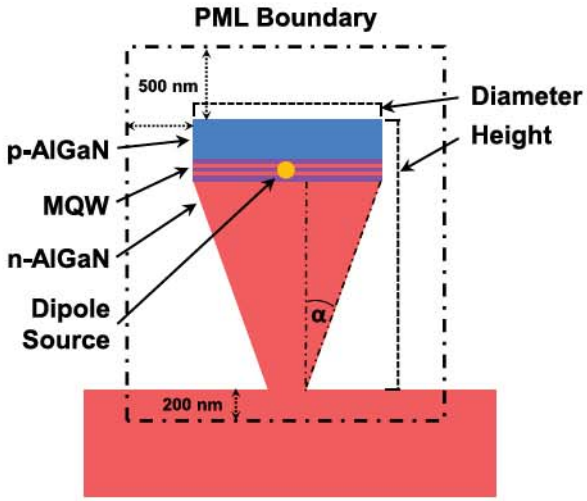

Fig. 2. Cross sectional schematic showing a generalized representation of a simulated nanowire.

just inside the domain boundaries to measure the luminous flux which escapes from the structure. Additional planar monitors are placed to intersect the structure along its axis in order to record electric and magnetic field intensities within the structure and in the space surrounding it. Extraction efficiency is determined by taking the ratio of luminous flux measured by various planar monitors to the full flux of the source. To determine the separate TE and TM-polarized extraction efficiencies, the results for the x and y-oriented dipole sources (TE) and the z-oriented dipole source (TM) were calculated separately. TE-polarized extraction efficiency was calculated by summing the luminous flux of the x and y-oriented dipoles measured by power monitors located at the edges of the domain and dividing this by the flux measured by the 20 nm volumetric monitor placed around the dipole source. TM-polarized emission was calculated similarly.

III. Results and Discussion

Our results show that narrower, taller structures yield higher η_{EXT}, and that the extraction efficiency of TM-polarized emission is larger than that of TE-polarized emission in these high AR structures. Fig. 3(a) shows the η_{EXT} of 1 μm, 2.5 μm, and 4 μm tall structures with diameters of 1 μm as a function of taper angle at an emission wavelength of 270 nm. Structures with no taper ($\alpha = 0\,^{\circ}$) tend exhibit extraction efficiencies of 40–45% for TM-polarized emission, and 28–40% for TE-polarized emission. η_{EXT} increases significantly with increasing taper angle as is shown in Fig. 3(a). This effect is most pronounced in taller structures (dashed and dotted lines), with extraction efficiencies of 98% being reached for TM-polarized emission from 4 μm tall, 1 μm diameter structures at a taper angle of 7°. Shorter, 1 μm tall structures require larger taper angles to reach these higher η_{EXT} values, but TM and TE extraction efficiencies of up to 92% and 78%, respectively, are likewise obtainable for these shorter structures at a taper angle of 20°. Fig. 3(a) plots the extraction efficiencies of shorter structures for larger taper angles than for taller structures due to geometric limitations.

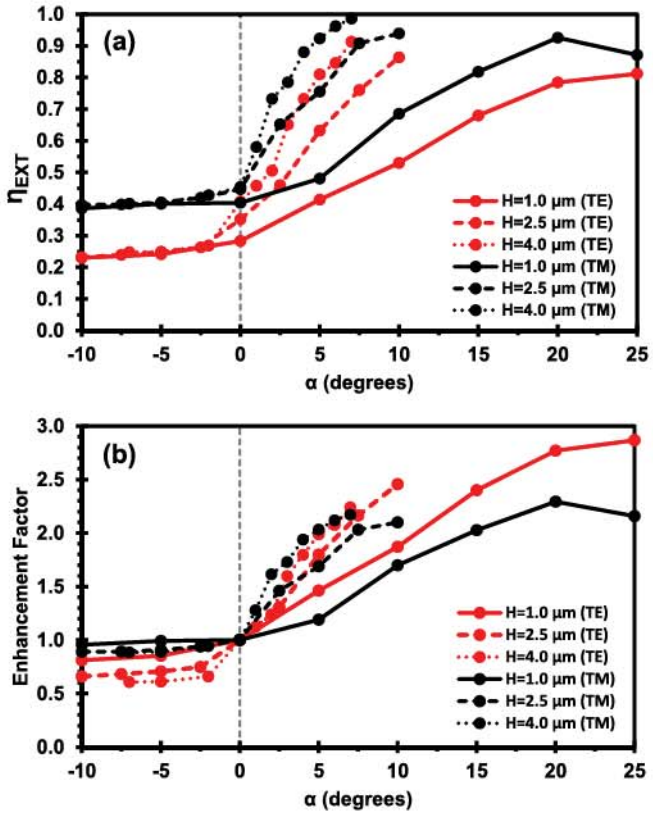

Fig. 3. η_{EXT} (a) and η_{EXT} enhancement factor (b) for TE (red) and TM (black) polarizations as a function of taper angle α for 1 μm tall (solid), 2.5 μm tall (dashed), and 4 μm tall (dotted) structures with diameters of 1 μm at $\lambda = 270$ nm.

While a 1 μm tall structure can be tapered to more than 25° before separating from the substrate, a 4 μm tall structure can only be tapered to slightly more than 7° before separation occurs. The maximum taper angle of a structure with diameter D and height H is given by $\alpha = \tan^{-1}(D/2H)$ when α is defined as shown in Fig. 2. The maximum taper angled plotted in Fig. 3(a) and (b) are 7° for 4 μm tall structures, 10° for 2.5 μm tall structures, and 25° for 1 μm tall structures. While positive taper angles are shown to produce significant increases in both TE- and TM-polarized η_{EXT} negative taper angles ($\alpha < 0\,^{\circ}$) appear to have the opposite effect, with all simulated negative taper angles producing small reductions in η_{EXT}. Interestingly, the extraction efficiencies of all three structure heights shown in Fig. 3(a) appear to quickly converge to the same values of ~39% for TM-polarized emission and 23% for TE-polarized emission at $\alpha = -10\,^{\circ}$. These results further reinforce the need to eliminate the flared bases ($\alpha < 0\,^{\circ}$) of dry-etched light emitting structures in order to improve η_{EXT}. Fig. 3(b) plots enhancement factor as a function of α in order to give a more qualitative representation of the change in η_{EXT} which could be expected between structures with non-zero tapers angles and those with $\alpha = 0\,^{\circ}$. The data in Fig. 3(b) is produced by dividing the values for all $\alpha \neq 0\,^{\circ}$ by the extraction efficiency at $\alpha = 0\,^{\circ}$ for each height and polarization.

While Fig. 3 shows that η_{EXT} can be improved by using structures with a positive taper, Figs. 4 and 5 show cross-sectional

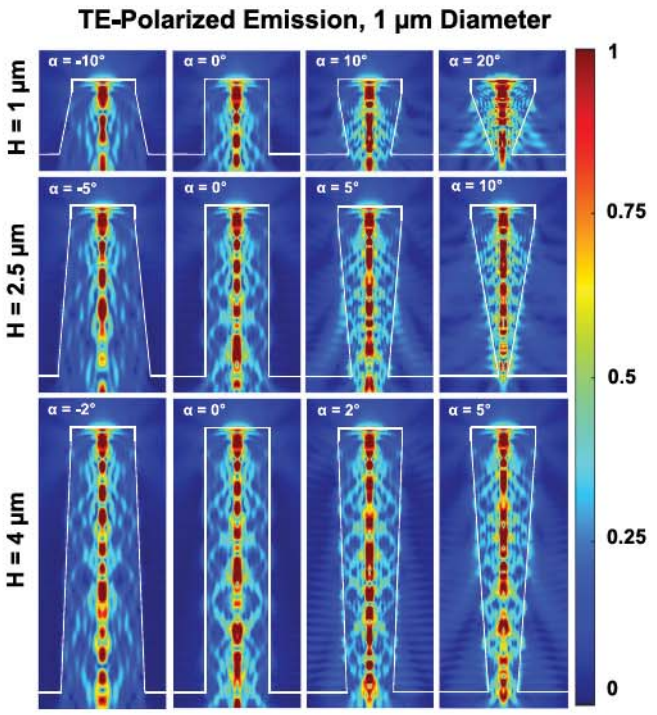

Fig. 4. Cross-sectional electric field intensity plots for 1 μm, 2.5 μm, and 4 μm tall structures with diameters of 1 μm and taper angles between $-10°$ and $20°$ for TE-polarized emission at $\lambda = 270$ nm.

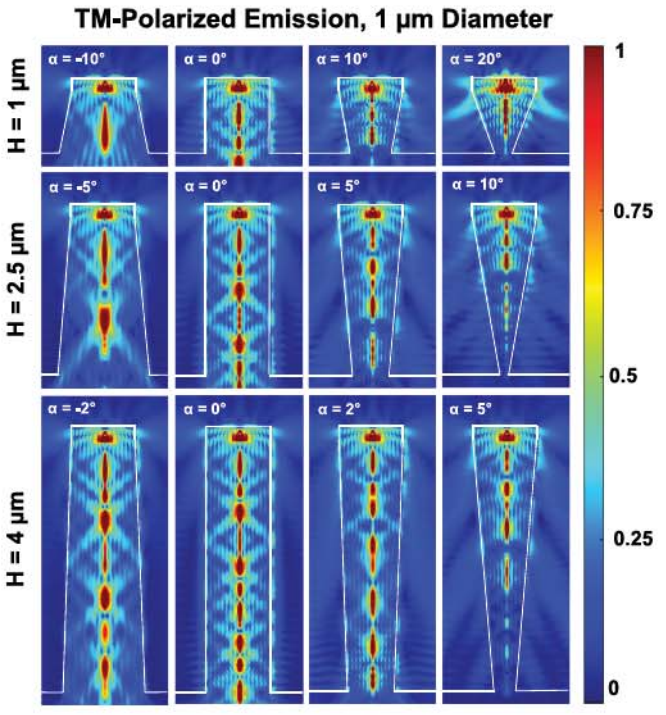

Fig. 5. Cross-sectional electric field intensity plots for 1 μm, 2.5 μm, and 4 μm tall structures with diameters of 1 μm and taper angles between $-10°$ and $20°$ for TM-polarized emission at $\lambda = 270$ nm.

electric field intensity plots which allow for better understanding of *why* positive taper improves extraction efficiency. The electric field intensities shown in Figs. 4 and 5 are captured by a monitor placed to bisect the simulated structures along their axis, with Fig. 4 showing the results for TE-polarized emission and Fig. 5 showing the results for TM-polarized emission. The structures shown in Figs. 4 and 5 are the same structures for which η_{EXT} data is presented in Fig. 3. Taper angles of $-10°$, $0°$, $10°$, and $20°$ are shown for 1 μm tall structures, $-5°$, $0°$, $5°$, and $10°$ for 2.5 μm tall structures, and $-2°$, $0°$, $2°$, and $5°$ for 4 μm tall structures. These cross-sectional electric field intensity plots allow for visualization of the optical modes which develop within these structures and identification of the directions in which light most efficiently extracted. It is immediately evident from Fig. 4 when comparing taper angles of $0°$, $10°$, and $20°$ that the optical modes which develop within the structures become more complex as taper angle is increased. For the TE-polarized emission shown in Fig. 4, the electric field intensities in free space near the sidewalls of all structures with no taper ($\alpha = 0°$) are effectively zero, indicating that almost no light is able to escape from the sidewalls of these structures. Results are similar for negative taper angles. In contrast, structures with positive taper exhibit much higher field intensities in the adjacent free space, indicating that extraction is able to occur more readily through the sidewalls of tapered structures even for TE-polarized emission, which prefers top extraction. It can also be seen that the direction in which light escapes from tapered structures is non-uniform, and appears to be influenced by the taper angle, structure height, and the location of optical modes on the axis of the structure. This effect is easiest to see in the 2.5 μm tall structure with a taper angle of $5°$, in which two "beams" can be seen projecting downward from near the midsection of the structure at an angle of $\sim 30°$. From Fig. 5, which shows TM-polarized emission, similar effects can be observed, however, in contrast to TE-polarized emission shown in Fig. 4, there are several notable differences. In the case of the TM-polarized emission shown in Fig. 5, sidewall emission is significant even in structures with no taper. This trend is expected since light which has transverse *magnetic* polarization with respect to the c-plane (the horizontal top surface of a structure) will have transverse *electric* polarization with respect to a vertical interface such as a structure sidewall. Likewise, the electric field intensity above the TM-emitting structures shown in Fig. 5 is effectively zero, whereas the TE-emitting structures shown in Fig. 4 have distinctively non-zero field intensity in the free space directly between them. While TM-polarized emission *can* be effectively extracted from vertical structures with no sidewall taper as shown in Fig. 5, positive taper angles can further enhance its extraction. The higher taper angle structures shown in Fig. 5 demonstrate that large increases in free space field intensity can be produced by taper angles as small as $2°$. As described for the TE-polarized emission in Fig. 4, variation of structure height and taper angle appear to affect the spatial distribution of sidewall emitted light in Fig. 5. For example, distinct regions of high electric field intensity can be easily seen for the 1 μm tall structure with $20°$ taper in Fig. 5. At very large taper angles in which the base of the structure is narrowed nearly to a point, the light lost into the substrate is massively reduced, an effect which can be best seen by comparing the 4 μm tall structures with taper angles of $0°$ and $5°$. In the structure with no taper, high electric field intensities

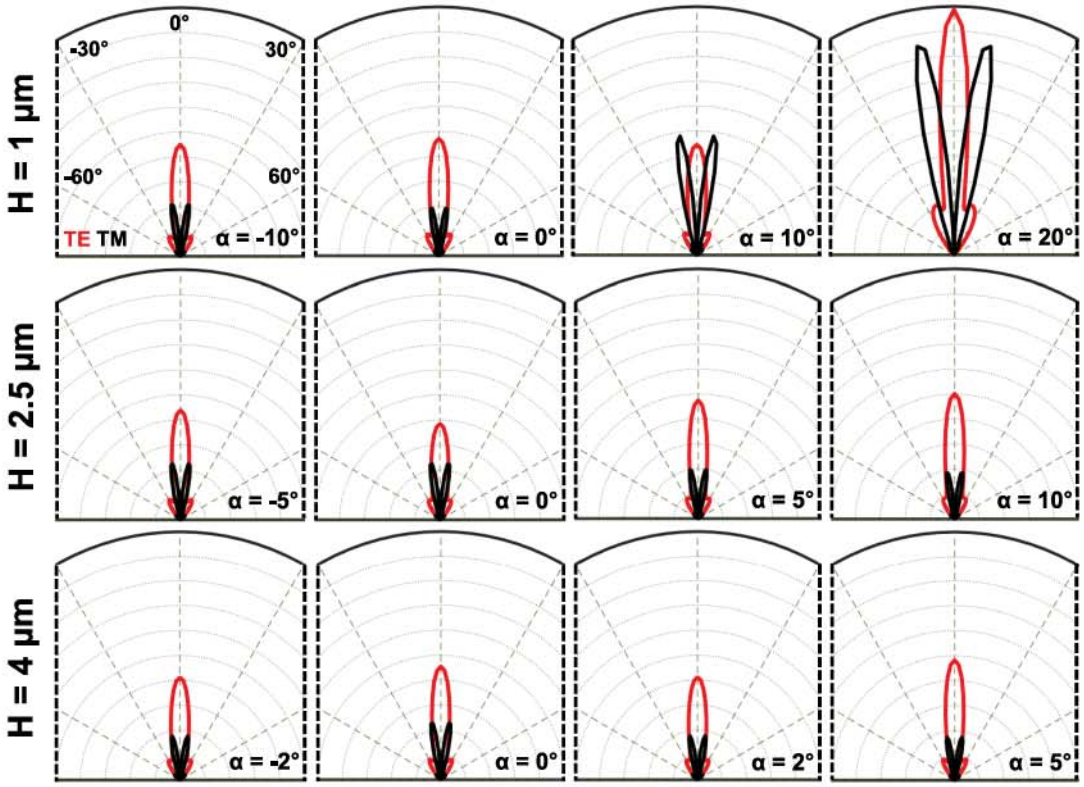

Fig. 6. Far-field emission patterns for TE-polarized (red) and TM-polarized (black) light, for 1 μm, 2.5 μm, and 4 μm tall structures with diameters of 1 μm and taper angles between $-10°$ and $20°$ at $\lambda = 270$ nm (the same structures whose electric field intensity plots are shown in Figs. 4 and 5).

can be seen in the substrate at the base of the structure, while in the structure with 5° taper, the field intensity is effectively zero through the substrate. The reduction of substrate light loss is due to the tapered sidewalls acting to confine emitted light to the upper portions of the structure where it can be extracted after one or multiple reflections instead of being lost into the substrate.

Fig. 6 presents the far field radiation plots of the structures shown in Figs. 3–5 in a polar format. The vertical axis of these plots represents the surface normal of the simulated structures, with each dashed line representing a 30° deflection from this surface normal. The red and black curves represent the intensities of TE and TM polarized radiation, respectively, which has escaped through the tops of the structures and is incident upon a monitor which is coplanar with the top of the simulation domain. As such, Fig. 6 only represents the distribution of light which has escaped from the tops of the structures, and does not consider sidewall emission. The far field patterns appear generally uniform for all structures, with a lambertian emission pattern for TE-polarized light and a "rabbit ears" emission pattern for TM-polarized light, both of which are consistent with existing literature [14], [40], [54]. The peak intensity of TE emission is generally 2-3x higher than that of TM-polarized emission, which is consistent with the well documented poor η_{EXT} TM-polarized light. However, this consistency breaks down for 1 μm tall structures with taper angles of 10° and 20°, in which the maximum intensity of TM-polarized emission approaches or exceeds that of TE-polarized emission. The increase in TM-polarized emission intensity in these two structures is due to their high taper angles relative to the other simulated structures, which serve to reflect downward emitted light back toward the top surface of these structures. The optical modes within these structures are also altered by their high taper angles which likely also contribute to modification of their far field radiation patterns. While the majority of light is extracted from the sidewalls of these structures, Fig. 6 shows that modification of the top-emitted far field radiation patterns is also possible in structures with high taper angles. Existing literature has shown that narrower, taller structures improve light extraction efficiency [14], [40], but it remains of interest to explore the effects of height and diameter in tapered structures. Fig. 7 shows TM (a) and TE (b) extraction efficiency as a function of structure height for diameters of 0.5 μm (dotted), μm (dashed), and 1.5 μm (solid) for a fixed taper angle of 10°. It is immediately evident that, in keeping with existing literature, η_{EXT} increases with the height of the structure. Of note are the very low extraction efficiencies of structures with ARs less than unity (height/diameter). These low extraction efficiencies are most noticeable for structures with diameters of 1 μm and 1.5 μm, whose extraction efficiencies drop from $\sim$60% at an AR of 1 to less than 30% at an AR of $\sim$0.1. Low extraction efficiency is expected from low AR structures because they are very similar to the mesas which are normally used in the fabrication of LEDs and which have been shown to have poor extraction efficiencies. Fig. 7 also shows a general trend of extraction efficiency increasing with decreasing diameter. While 0.5 μm diameter structures consistently have the highest η_{EXT}

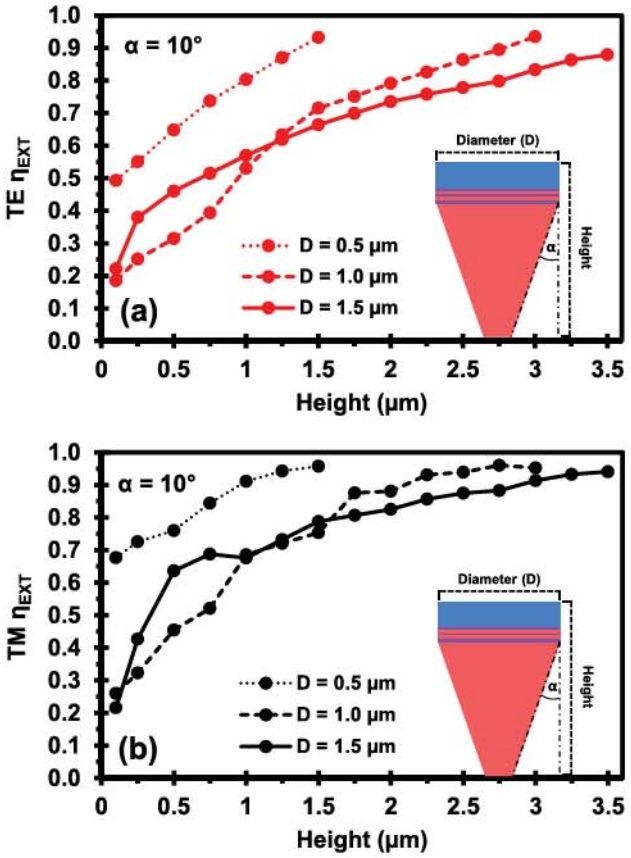

Fig. 7. η_{EXT} for TM (a) and TE (b) polarizations as a function of height for structures with diameters of 0.5 μm, 1 μm, and 1.5 μm and (solid), 2.5 μm tall (dashed), and 4 μm tall (dotted) structures with diameters of 1 μm at $\lambda =$ 270 nm.

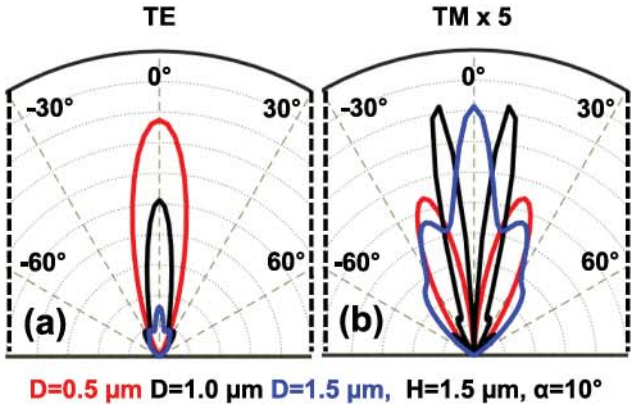

Fig. 8. Far-field emission patterns for TE-polarized (a) and TM-polarized (b) light for 0.5 μm, 1 μm, and 1.5 μm diameter structures with a height at 1.5 μm and a taper angle of 10° at $\lambda = 270$ nm. TM-polarized emission (b) is multiplied by a factor of 5 to better show the emission pattern.

at a given height, 1.5 μm diameter structures actually appear to have higher extraction efficiencies than 1 μm diameter structures at heights less than 1.5 μm. This observation holds true for both TM and TE polarizations, and is likely due the nature of the optical modes which develop within 1 μm and 1.5 μm tall structures of within this height range.

Fig. 8 shows the top emission far-field polar radiation plots for 0.5 μm (red), 1 μm (black), and 1.5 μm (blue) diameter structures with heights of 1.5 μm and taper angles of 10°. The intensity of TE-polarized emission parallel to the surface normal appears to increase as the diameter of the structure decreases. This trend, which was also confirmed by the far-field emission patterns for additional diameters, is likely due to increased confinement of light in narrower structures which magnifies top emission of TE-polarized light while reducing sidewall emission. No such pattern is observed for TM-polarized emission, as each structure has approximately the same peak emission intensity, likely due to the vast majority of extraction occurring through the sidewalls. This can be attributed to alteration of the optical modes within the structures which changes the angles at which light is most effectively out-coupled through the top of the structures. Note that the TM-polarized far-field patterns in Fig. 8 have been scaled up by a factor of 5 in order to make them easier to compare to one another. The far-field emission patterns for TM-polarized emission change significantly with diameter.

The structures explored thus far have been mostly in the "microstructure" regime, with dimensions of approximately 1 μm or greater. For DUV emission, these can be considered "super-wavelength" structures, as their dimensions are generally much larger than the wavelength of the emitted light (270 nm). It is also of interest of explore "nanostructures," with near or subwavelength dimensions closer to the wavelength of the emitted light in order to determine if the effects of height, diameter, and taper angle change for these smaller structures. Fig. 9 compares the extraction efficiencies (a) and extraction efficiency enhancement factors (b) for 1 μm tall, 1 μm diameter structures (solid), and 500 nm tall, 500 nm diameter structures (dashed) as a function of taper angle. All structures have an AR of 1. TM-polarized η_{EXT} is shown in black, while TE-polarized η_{EXT} is shown in red. It is immediately evident that, despite the identical aspect ratios of these two sets of structures, the larger 1 μm structures benefit far more from higher taper angles than the 500 nm structures. For example, at 20°, the TM extraction efficiency of the 1 μm structure is enhanced by around 2.3x, while the TM extraction efficiency of the 500 nm structure is enhanced by only 1.25x. As can be seen from Fig. 9(a), this is due mostly to the initial ($\alpha = 0°$) TM η_{EXT} of the 500 nm structure being much higher (69%) than that of the 1 μm structure (40%). A similar trend is evident for TE-polarized emission, with 500 nm structures seeing almost no enhancement with increasing taper angles while 1 μm structures can achieve enhancements in excess of 2x at taper angles of 20°. Smaller improvements to extraction efficiency are realized in smaller structures as taper angle is increased simply because η_{EXT} is inherently higher in smaller structures leaving less room for improvement. The key takeaway from this comparison is that extraction can be improved either through use of smaller structures with little to no taper, or larger structures with higher taper angles.

Fig. 10 shows the extraction efficiencies (a) and extraction efficiency enhancement factors (b) for four different nanostructure sizes. 500/100 nm tall/diameter nanostructures are represented by diamonds and solid lines, 500/500 nm nanostructures by circles and long dashed lines, 1000/100 nm nanostructures by

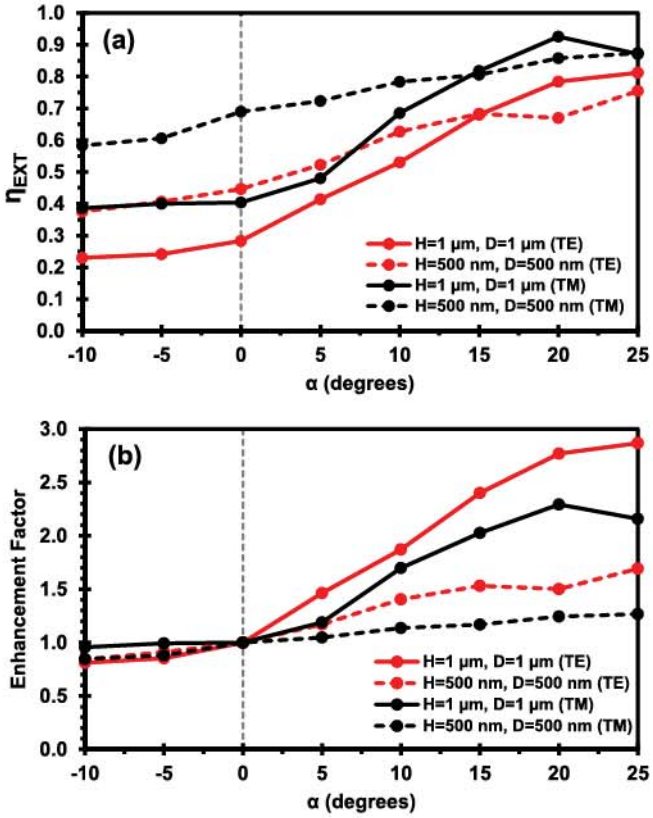

Fig. 9. η_{EXT} (a) and η_{EXT} enhancement factor (b) for TE (red) and TM (black) polarizations as a function of taper angle α for 1 μm tall, 1 μm diameter structures (solid), and 500 nm tall, 500 nm diameter structures (dashed) at $\lambda = 270$ nm. Both structures have ARs of 1 (height/diameter).

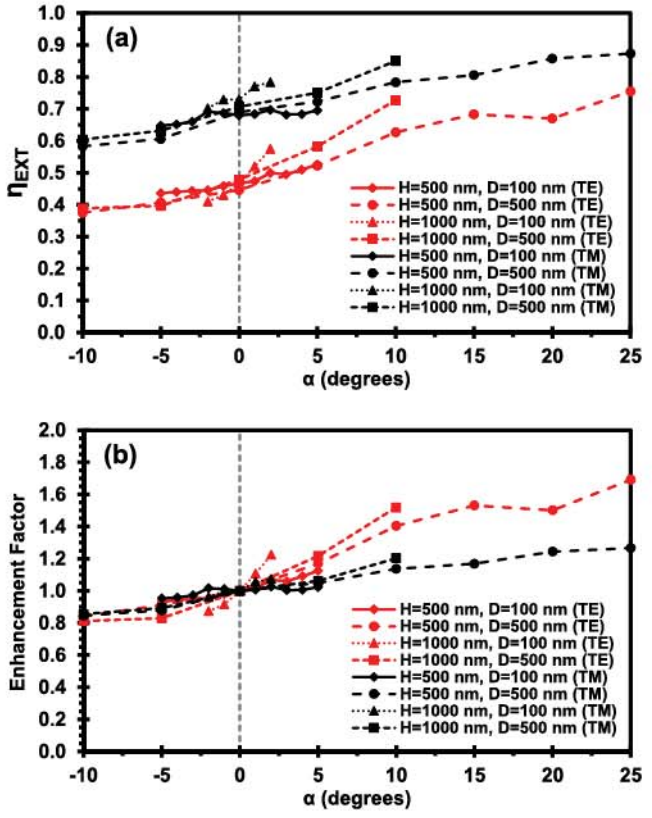

Fig. 10. η_{EXT} (a) and η_{EXT} enhancement factor (b) for TE (red) and TM (black) polarizations as a function of taper angle α for 500/100 nm tall/diameter (diamond), 500/500 nm (circle), 1000/100 nm (triangle), and 1000/500 nm (square) structures at $\lambda = 270$ nm.

triangles and dotted lines, and 1000/500 nm nanostructures by squares and short dashed lines. TE and TM polarizations are shown in red and black respectively. It can be seen from Fig. 10(a) that TE-polarized emission benefits significantly more from higher taper angles than TM-polarized emission. This trend was not observed in the larger microstructures described previously, however the magnitude of enhancement for TE-polarized extraction efficiency is still lower in these nanostructures than it is in microstructures at equivalent taper angles. This trend is in keeping with our previous observation that larger structures almost universally benefit more from higher taper angles. It can also be seen when comparing Figs. 10(a) and 3(a) that the difference between TE and TM polarized extraction efficiency at $\alpha = 0\,^\circ$ is larger for nanostructures than for microstructures. In Fig. 3(a) η_{EXT} at $\alpha = 0\,^\circ$ increases from an average of around 35% for TE polarized emission to around 45% for TM polarized emission, a difference of around 10%. This difference increases to around 25% in Fig. 10(a), showing that η_{EXT} is more sensitive to the polarization of emitted light in smaller structures.

Cross-sectional electric field intensity plots at select taper angles for 100 nm diameter nanostructures are shown in Fig. 11. As in Figs. 4 and 5, structures with no sidewall taper exhibit very low TE polarized field intensities in the free space near the structure sidewalls, indicating that extraction of TE-polarized light from the sidewalls is negligible in these structures. Results are again similar for negative taper angles. As in Fig. 4, TE-emitting structures with positive taper angles show much higher field intensities in the free space adjoining their sidewalls, indicating that extraction through the sidewalls in enhanced by even very small taper angles for TE-polarized emission. In contrast, and in keeping with the results shown in Fig. 10, TM-polarized emission appears less affected by positive taper angles. As TM-polarized emission is already easily extracted from structures with such small diameters, there is little room for extraction to be further improved by the addition of small positive taper angles. As shown in Figs. 4 and 5, structures with close to their maximum taper angle with very small base diameters can be seen to lose significantly less light into the substrate. This is especially noticeable in Fig. 11 for TE-polarized emission. From Fig. 11 it can also be seen these narrower, "subwavelength" 100 nm diameter structures are much more sensitive to the development of confined optical modes than larger structures. In the top half of Fig. 11, which shows results for TE-polarized emission, all nanostructures have extremely high internal electric field intensities. Even very small increases in taper angle serve to drastically increase the field intensity in some regions. Note also that the maxima of the scale bar in Fig. 11 is doubled with respect to Figs. 4 and 5 in order to make the optical modes visible. While confinement of TE-polarized emission seems to be much greater in these smaller structures, TM-polarized emission appears unaffected, as it is easily extracted from the

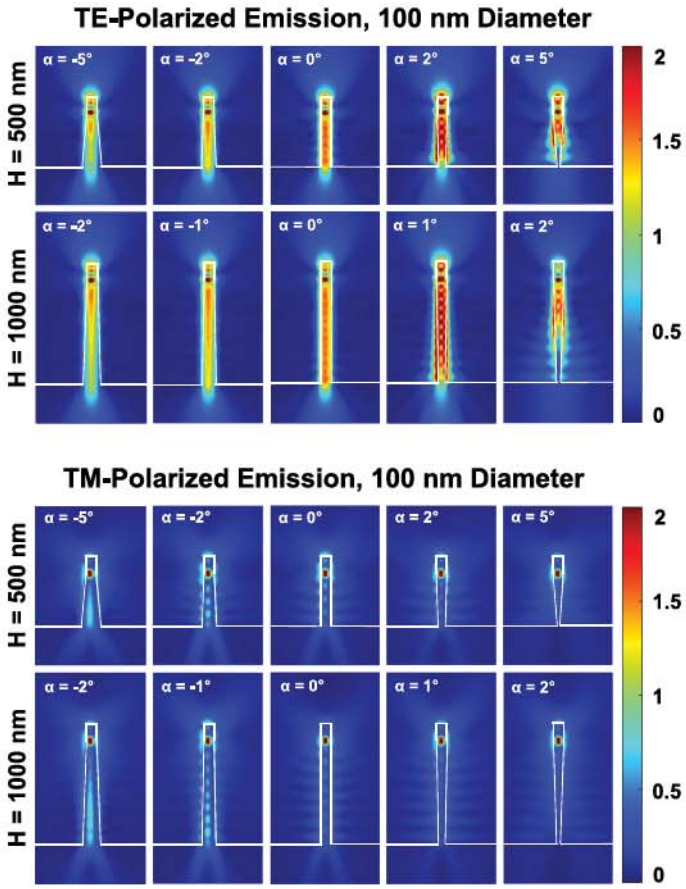

Fig. 11. Cross-sectional electric field intensity plots for 500 nm and 1000 nm tall structures with diameters of 100 nm and taper angles between $-5°$ and $5°$ for TE-polarized (top) and TM-polarized (bottom) emission at $\lambda = 270$ nm. Field intensity is halved in comparison to Figs. 4, 5, and 12 to ensure optical modes can be seen.

sidewalls, making it far less dependent on the size and taper angle of these nanostructures. The key conclusion of this analysis of nanostructures vs microstructures is that larger structures stand to benefit much more from an inverse taper profile, while smaller structures, which have inherently high extraction efficiency, see more limited improvements at equivalent taper angles. Additionally, the optical modes which develop within these structures likely play a key role the extraction of light from near and subwavelength structures, while larger microstructures are less susceptible to this influence.

IV. Conclusion

In conclusion, light extraction from both AlGaN microstructures and nanostructures was investigated at 270 nm using FDTD simulations in order to better understand the effects on η_{EXT} of parameters such structure height, diameter, and taper angle. Results showed that significant improvements to η_{EXT} can be obtained through use of an "inverse taper," in which the base of the structure is narrowed relative to the top of the structure. In the case of microstructures with diameters of 1 μm and heights > 1 μm, η_{EXT} was shown to be increased from around 45% to more than 95% (a 2.1x enhancement) for TM-polarized emission, and from around 35% to more than 85% (a 2.4x enhancement) for TE-polarized emission by a taper of only $5°$. Cross-sectional electric field intensity plots visually illustrate how tapered sidewalls improve the extraction of light into free space and depict the variations in the internal optical modes which occur as the size and taper angle of these structures are changed. In smaller nanostructures the effects of an inverse taper were found to be less significant, due to primarily to the intrinsically higher extraction efficiencies of structures with diameters <500 nm. In comparison to microstructures, in which extraction efficiency enhancements of more than 2x could be achieved at a taper of only $5°$, no more than 1.2x enhancement was realized for nanostructures at the same angle. In keeping with the findings of other publications, our results also show that η_{EXT} can also be increased by reducing the diameters of light emitting structures or by increasing their height. Light extraction has long been the single most significant bottleneck preventing the development of high EQE DUV LEDs. The findings of this simulation study, along with our recent discovery of a method to reliably fabricate high Al-content AlGaN micro and nanostructures with specific taper angles, lay the groundwork for development of record high EQE DUV LEDs based on arrays of high aspect ratio light emitting structures with extremely high light extraction efficiencies.

References

[1] H. Amano et al., "The 2020 UV emitter roadmap," *J. Phys. D: Appl. Phys.*, vol. 53, no. 50, Dec. 2020, Art. no. 503001.

[2] S. Zhao, J. Lu, X. Hai, and X. Yin, "AlGaN nanowires for ultraviolet light-emitting: Recent progress, challenges, and prospects," *Micromachines*, vol. 11, no. 2, Jan. 2020, Art. no. 125.

[3] E. F. Schubert, *Light-Emitting Diodes*, 2nd ed. Cambridge, U.K.: Cambridge Univ. Press, 2006.

[4] M. Kneissl et al., "Advances in group III-nitride-based deep UV light-emitting diode technology," *Semicond. Sci. Technol.*, vol. 26, no. 1, Jan. 2011, Art. no. 014036.

[5] M. Kneissl, T.-Y. Seong, J. Han, and H. Amano, "The emergence and prospects of deep-ultraviolet light-emitting diode technologies," *Nature Photon.*, vol. 13, no. 4, pp. 233–244, Apr. 2019.

[6] M. Raeiszadeh and B. Adeli, "A critical review on ultraviolet disinfection systems against COVID-19 outbreak: Applicability, validation, and safety considerations," *ACS Photon.*, vol. 7, no. 11, pp. 2941–2951, Nov. 2020.

[7] A. Wiedenmann, B. Fischer, U. Straub, C.-H. Wang, B. Flehmig, and D. Schoenen, "Disinfection of hepatitis a virus and MS-2 coliphage in water by ultraviolet irradiation: Comparison of UV-susceptibility," *Water Sci. Technol.*, vol. 27, no. 3/4, pp. 335–338, Feb. 1993.

[8] Y. Gerchman, H. Mamane, N. Friedman, and M. Mandelboim, "UV-LED disinfection of coronavirus: Wavelength effect," *J. Photochem. Photobiology B: Biol.*, vol. 212, Nov. 2020, Art. no. 112044.

[9] M. Auf der Maur, A. Pecchia, G. Penazzi, W. Rodrigues, and A. Di Carlo, "Efficiency drop in green InGaN /GaN light emitting diodes: The role of random alloy fluctuations," *Phys. Rev. Lett.*, vol. 116, no. 2, Jan. 2016, Art. no. 027401.

[10] T. Takano, T. Mino, J. Sakai, N. Noguchi, K. Tsubaki, and H. Hirayama, "Deep-ultraviolet light-emitting diodes with external quantum efficiency higher than 20% at 275 nm achieved by improving light-extraction efficiency," *Appl. Phys. Exp.*, vol. 10, no. 3, Feb. 2017, Art. no. 031002.

[11] S. Hagedorn, A. Knauer, F. Brunner, A. Mogilatenko, U. Zeimer, and M. Weyers, "High-quality AlN grown on a thermally decomposed sapphire surface," *J. Cryst. Growth*, vol. 479, pp. 16–21, Dec. 2017.

[12] C. Liu et al., "High internal quantum efficiency from AlGaN-delta-GaN quantum well at 260 nm," in *Proc. Conf. Lasers Electro-Opt.*, May 2020, Paper AF1I.2.

[13] D. Feezell and S. Nakamura, "Invention, development, and status of the blue light-emitting diode, the enabler of solid-state lighting," *Comput. Rendus Physique*, vol. 19, no. 3, pp. 113–133, Mar. 2018.

[14] Y. K. Ooi, C. Liu, and J. Zhang, "Analysis of polarization-dependent light extraction and effect of passivation layer for 230-nm AlGaN nanowire light-emitting diodes," *IEEE Photon. J.*, vol. 9, no. 4, Aug. 2017, Art. no. 4501812.

[15] Y. Kashima et al., "High external quantum efficiency (10%) algan-based deep-ultraviolet light-emitting diodes achieved by using highly reflective photonic crystal on p-AlGaN contact layer," *Appl. Phys. Exp.*, vol. 11, no. 1, Jan. 2018, Art. no. 012101.

[16] R. Lin et al., "Tapering-induced enhancement of light extraction efficiency of nanowire deep ultraviolet LED by theoretical simulations," *Photon. Res.*, vol. 6, no. 5, May 2018, Art. no. 457.

[17] H.-Y. Ryu, I.-G. Choi, H.-S. Choi, and J.-I. Shim, "Investigation of light extraction efficiency in AlGaN deep-ultraviolet light-emitting diodes," *Appl. Phys. Exp.*, vol. 6, no. 6, Jun. 2013, Art. no. 062101.

[18] W. Guo et al., "Enhancing light coupling and emission efficiencies of AlGaN thin film and AlGaN/GaN multiple quantum wells with periodicity-wavelength matched nanostructure array," *Nanoscale*, vol. 9, no. 40, pp. 15477–15483, 2017.

[19] M. Khizar, Z. Y. Fan, K. H. Kim, J. Y. Lin, and H. X. Jiang, "Nitride deep-ultraviolet light-emitting diodes with microlens array," *Appl. Phys. Lett.*, vol. 86, no. 17, Apr. 2005, Art. no. 173504.

[20] R. Liang et al., "High light extraction efficiency of deep ultraviolet LEDs enhanced using nanolens arrays," *IEEE Trans. Electron Devices*, vol. 65, no. 6, pp. 2498–2503, Jun. 2018.

[21] N. Maeda, M. Jo, and H. Hirayama, "Improving the efficiency of AlGaN deep-UV LEDs by using highly reflective Ni/Al p-type electrodes," *Phys. Status Solidi A*, vol. 215, no. 8, Apr. 2018, Art. no. 1700435.

[22] M. Djavid and Z. Mi, "Enhancing the light extraction efficiency of AlGaN deep ultraviolet light emitting diodes by using nanowire structures," *Appl. Phys. Lett.*, vol. 108, no. 5, Feb. 2016, Art. no. 051102.

[23] M. Djavid et al., "Effects of optical absorption in deep ultraviolet nanowire light-emitting diodes," *Photon. Nanostructures - Fundamentals Appl.*, vol. 28, pp. 106–110, Feb. 2018.

[24] S. Zhao et al., "Molecular beam epitaxy growth of Al-rich AlGaN nanowires for deep ultraviolet optoelectronics," *APL Mater.*, vol. 4, no. 8, Aug. 2016, Art. no. 086115.

[25] S. Zhao, S. Sadaf, X. Liu, and Z. Mi, "AlGaN nanowire deep ultraviolet optoelectronics," in *Proc. IEEE Photon. Soc. Summer Topical Meeting Ser.*, 2017, pp. 87–88.

[26] S. Zhao et al., "Aluminum nitride nanowire light emitting diodes: Breaking the fundamental bottleneck of deep ultraviolet light sources," *Sci. Rep.*, vol. 5, no. 1, Jul. 2015, Art. no. 8332.

[27] S. M. Sadaf et al., "An AlGaN core–shell tunnel junction nanowire light-emitting diode operating in the ultraviolet-c band," *Nano. Lett.*, vol. 17, no. 2, pp. 1212–1218, Feb. 2017.

[28] S. Zhao, S. M. Sadaf, S. Vanka, Y. Wang, R. Rashid, and Z. Mi, "Sub-milliwatt AlGaN nanowire tunnel junction deep ultraviolet light emitting diodes on silicon operating at 242 nm," *Appl. Phys. Lett.*, vol. 109, no. 20, Nov. 2016, Art. no. 201106.

[29] H. Sun et al., "Surface-Passivated AlGaN nanowires for enhanced luminescence of ultraviolet light emitting diodes," *ACS Photon.*, vol. 5, no. 3, pp. 964–970, Mar. 2018.

[30] H. Q. T. Bui et al., "High-performance nanowire ultraviolet light-emitting diodes with potassium hydroxide and ammonium sulfide surface passivation," *Appl. Opt.*, vol. 59, no. 24, Aug. 2020, Art. no. 7352.

[31] M. S. Alias et al., "Enhancing the light-extraction efficiency of an AlGaN nanowire ultraviolet light-emitting diode by using nitride/air distributed bragg reflector nanogratings," *IEEE Photon. J.*, vol. 9, no. 5, Oct. 2017, Art. no. 4900508.

[32] S. Zhao, M. Djavid, and Z. Mi, "Surface emitting, high efficiency near-vacuum ultraviolet light source with aluminum nitride nanowires monolithically grown on silicon," *Nano Lett.*, vol. 15, no. 10, pp. 7006–7009, Oct. 2015.

[33] T. F. Kent, S. D. Carnevale, A. T. M. Sarwar, P. J. Phillips, R. F. Klie, and R. C. Myers, "Deep ultraviolet emitting polarization induced nanowire light emitting diodes with $Al_x Ga_{1-x} N$ active regions," *Nanotechnology*, vol. 25, no. 45, Nov. 2014, Art. no. 455201.

[34] Z. Mi et al., "Molecular beam epitaxial growth and characterization of Al(Ga)N nanowire deep ultraviolet light emitting diodes and lasers," *J. Phys. D: Appl. Phys.*, vol. 49, no. 36, Sep. 2016, Art. no. 364006.

[35] R. T. Velpula, B. Jain, M. R. Philip, H. D. Nguyen, R. Wang, and H. P. T. Nguyen, "Epitaxial growth and characterization of alinn-based core-shell nanowire light emitting diodes operating in the ultraviolet spectrum," *Sci. Rep.*, vol. 10, no. 1, Dec. 2020, Art. no. 2547.

[36] Y. Ra, S. Kang, and C. Lee, "Ultraviolet light-emitting diode using nonpolar AlGaN core–shell nanowire heterostructures," *Adv. Opt. Mater.*, vol. 6, no. 14, Jul. 2018, Art. no. 1701391.

[37] A. T. M. G. Sarwar, B. J. May, J. I. Deitz, T. J. Grassman, D. W. McComb, and R. C. Myers, "Tunnel junction enhanced nanowire ultraviolet light emitting diodes," *Appl. Phys. Lett.*, vol. 107, no. 10, Sep. 2015, Art. no. 101103.

[38] H.-Y. Ryu, "Evaluation of light extraction efficiency of gan-based nanorod light-emitting diodes by averaging over source positions and polarizations," *Crystals*, vol. 8, no. 1, Jan. 2018, Art. no. 27.

[39] J. Chesin, X. Zhou, and S. Gradečak, "Light extraction in individual GaN nanowires on Si for LEDs," *Proc. SPIE*, vol. 8467, Oct. 2012, Art. no. 846703.

[40] H.-Y. Ryu, "Large enhancement of light extraction efficiency in algan-based nanorod ultraviolet light-emitting diode structures," *Nanoscale Res. Lett.*, vol. 9, no. 1, Dec. 2014, Art. no. 58.

[41] Z. Fang et al., "Si donor incorporation in GaN nanowires," *Nano Lett.*, vol. 15, no. 10, pp. 6794–6801, Oct. 2015.

[42] N. H. Tran, B. H. Le, S. Zhao, and Z. Mi, "On the mechanism of highly efficient p-type conduction of Mg-doped ultra-wide-bandgap AlN nanostructures," *Appl. Phys. Lett.*, vol. 110, no. 3, Jan. 2017, Art. no. 032102.

[43] B. J. May, A. T. M. G. Sarwar, and R. C. Myers, "Nanowire LEDs grown directly on flexible metal foil," *Appl. Phys. Lett.*, vol. 108, no. 14, Apr. 2016, Art. no. 141103.

[44] F. Glas, "Critical dimensions for the plastic relaxation of strained axial heterostructures in free-standing nanowires," *Phys. Rev. B*, vol. 74, no. 12, Sep. 2006, Art. no. 121302.

[45] M. Hartensveld, B. Melanson, C. Liu, and J. Zhang, "AlGaN nanowires with inverse taper for flexible DUV emitters," *J. Phys. Photon.*, vol. 3, no. 2, Apr. 2021, Art. no. 024016.

[46] B. Melanson, M. Hartensveld, C. Liu, and J. Zhang, "Realization of electrically driven AlGaN micropillar array deep-ultraviolet light emitting diodes at 286 nm," *AIP Adv.*, vol. 11, no. 9, Sep. 2021, Art. no. 095005.

[47] G. T. Wang, B. Leung, M.-C. Tsai, K. R. Sapkota, B. A. Kazanowska, and K. S. Jones, "Top-Down etch processes for III-nitride nanophotonics," in *Proc. IEEE Photon. Conf.*, 2019, pp. 1–2.

[48] W. Chen, J. Lin, G. Hu, and B. Zhang, "GaN nanowire fabricated by selective wet-etching of GaN micro truncated-pyramid," *J. Cryst. Growth*, vol. 426, 2015, Art. no. 168.

[49] D. A. Stocker, E. F. Schubert, and J. M. Redwing, "Crystallographic wet chemical etching of GaN," *Appl. Phys. Lett.*, vol. 73, no. 18, pp. 2654–2656, Nov. 1998.

[50] M. Hartensveld, G. Ouin, C. Liu, and J. Zhang, "Effect of KOH passivation for top-down fabricated InGaN nanowire light emitting diodes," *J. Appl. Phys.*, vol. 126, no. 18, 2019, Art. no. 183102.

[51] A. J. Jackson and A. Walsh, "Oxidation of GaN: An *ab initio* thermodynamic approach," *Phys. Rev. B*, vol. 88, no. 16, Oct. 2013, Art. no. 165201.

[52] Y.-W. Jo et al., "AlGaN/GaN FinFET with extremely broad transconductance by side-wall wet etch," *IEEE Electron Device Lett.*, vol. 36, no. 10, pp. 1008–1010, Oct. 2015.

[53] K.-S. Im et al., "Lateral GaN nanowire prepared by using two-step TMAH wet etching and HfO2 sidewall spacer," *J. Cryst. Growth*, vol. 441, pp. 41–45, May 2016.

[54] A.-L. Henneghien, B. Gayral, Y. Désières, and J.-M. Gérard, "Simulation of waveguiding and emitting properties of semiconductor nanowires with hexagonal or circular sections," *J. Opt. Soc. Am. B*, vol. 26, no. 12, Dec. 2009, Art. no. 2396.

[55] Y. Zhang et al., "Enhancing both TM- and TE-Polarized light extraction efficiency of algan-based deep ultraviolet light-emitting diode via air cavity extractor with vertical sidewall," *IEEE Photon. J.*, vol. 10, no. 4, Aug. 2018, Art. no. 8200809.

[56] W.-K. Chen, Ed., "Computational electromagnetic: The finite-difference time-domain method," in *The Electrical Engineering Handbook*. New York, NY, USA: Academic, 2005, pp. 629–670.

[57] A. Taflove and S. C. Hagness, *Computational Electrodynamics: The Finite-Difference Time-Domain Method*. Norwood, MA, USA: Artech House, 2005.

[58] FullWAVE"Synopsys's Optical Solutions Group," 2022. [Online]. Available: https://optics.synopsis.com

[59] G. Yu et al., "Optical properties of wurtzite structure GaN on sapphire around fundamental absorption edge (0.78–4.77 eV) by spectroscopic ellipsometry and the optical transmission method," *Appl. Phys. Lett.*, vol. 70, no. 24, pp. 3209–3211, Jun. 1997.

[60] M. Tian et al., "Enhanced light extraction of the deep-ultraviolet micro-LED via rational design of chip sidewall," *Opt. Lett.*, vol. 46, no. 19, Oct. 2021, Art. no. 4809.

[61] H. Yu et al., "Development of highly efficient ultraviolet LEDs on hybrid patterned sapphire substrates," *Opt. Lett.*, vol. 46, no. 21, Nov. 2021, Art. no. 5356.